Multi-Orbital-Angular-Momentum-Mode Vortex Wave Multiplexing and Demultiplexing with Shared-Aperture Reflective Metasurfaces

Qiang Feng,[1] Xudong Kong,[1] Mingming Shan,[1] Yifeng Lin,[1] Long Li,[1,*] and Tie Jun Cui[2,3,†]

[1] *Key Laboratory of High Speed Circuit Design and EMC, Ministry of Education, School of Electronic Engineering, Xidian University, Xi'an 710071, China*

[2] *State Key Laboratory of Millimeter Waves, Southeast University, Nanjing 210096, China*

[3] *School of Electronic Engineering, Xidian University, Xi'an 710071, China*

(Received 6 December 2021; revised 7 February 2022; accepted 11 February 2022; published 7 March 2022)

As an alternative degree of freedom for wireless communications, orbital angular momentum (OAM) multiplexing and demultiplexing can be applied to achieve higher communication capacity. Metasurface has advanced ability to manipulate electromagnetic (EM) waves, and has gradually become an enabling EM technology for future wireless communications. It is meaningful and useful to combine the advantages of OAM and metasurfaces. Here we propose a multi-OAM-mode vortex wave multiplexing and demultiplexing scheme based on shared-aperture reflective metasurface. The specifically designed reflective metasurface can realize the corresponding OAM-mode modulations and demodulations of different incident carrier waves in the corresponding data channels. By modulating multiple data channels on multiple OAM modes, the multiplication of the communication capacity could be achieved. A prototype operating at microwave frequencies is designed, simulated, and fabricated for proof-of-concept illustration. To validate the OAM multiplexing and demultiplexing scheme, we conduct dual-channel OAM-mode transmission experiments, in which two shared-aperture reflective metasurfaces are adopted as the transmitter and receiver, respectively. This work paves the way for the metasurface-based OAM communication applications in future wireless communication technologies.

DOI: 10.1103/PhysRevApplied.17.034017

I. INTRODUCTION

Since the seminal papers in 1992 and 2007 [1,2], orbital angular momentum (OAM) has gained much interest in many research fields, especially in wireless communications. As an alternative degree of freedom, OAM can be used for increasing communication capacity by simultaneously transmitting multiple orthogonal OAM-mode vortex beams [3–6]. Theoretically, these different OAM modes are orthogonal and infinite, which are useful properties for the communications. The beams with different OAM modes, termed as vortex beams, are orthogonal to each other, which means that they carry multiple independent data streams and transmit simultaneously in free space [7,8]. Thus, the transmission capacity of the communication system can be increased multiple times through OAM multiplexing, and research teams in universities and enterprises all over the world have researched the related topics [9–12]. This OAM-mode multiplexing method is also called mode-division multiplexing (MDM), which is a subset of space-division multiplexing [13–15]. Another application method of OAM orthogonality is that different OAM modes can be used as data coding and decoding schemes [16,17], and this idea is more often adopted in quantum communications [18]. In addition, OAM vortex waves also show great application prospects in microwave sensing, radar imaging, and antenna pattern-shaping design [19–23]. Since OAM-mode vortex beam was proposed, it has experienced many controversies for its applications in communications [6,15,24–27]. However, as a developing research object but also with reliable physical background, it has unusual electromagnetic (EM) characteristics in beam shape and angular momentum[28,29]. Currently, its potential researches and applications are still promising and attractive [6,15,18,27,30–34].

Antenna technologies are applied for generating and receiving OAM vortex beams. Various radio-frequency OAM antennas have been studied, as reviewed in Ref. [35]. Meanwhile, EM metamaterials or metasurfaces have advanced EM-wave-manipulation abilities [36–38], which show great potentials in OAM vortex-beam manipulations [39–46]. However, most of the current OAM metasurface antennas simply focus on OAM beam generation and manipulation, without further considering its application scenarios and requirements in actual communication systems. Although some

*lilong@mail.xidian.edu.cn
†tjcui@seu.edu.cn

metasurface-based design schemes were proposed for multiple OAM-mode multiplexing [47,48], their OAM-mode multiplexing efficiency is discounted, i.e., the multiplexed OAM mode number is few. In Ref. [47], two different OAM modes were multiplexed, but it actually was realized by polarization multiplexing. In Ref. [48], both polarization multiplexing and OAM-mode multiplexing were considered to realize four OAM-mode multiplexing, but this holographic metasurface was not designed from the perspective of further practical applications. Most recently, a millimeter wave holographic flat lens antenna for OAM multiplexing was presented [49], however, it mainly focused on vortex-beam generation, and no more OAM multiplexing and demultiplexing transceiver analyses and experiments were carried out.

In this paper, we propose a multiple OAM-mode multiplexing and demultiplexing scheme using a multichannel shared-aperture reflective metasurface. Independently incident radio-frequency carrier-wave signals from the feeding horns can be modulated and demodulated through the specifically designed shared-aperture reflective metasurface. Because of the same metasurface design theories basis, this scheme could also be developed in an information metamaterial system and intelligent reflective surfaces (IRSs) [45,50,51]. We organize the paper as follows. Section II is the basic principle of the multiple OAM-mode vortex-beam multiplexing with multichannel shared-aperture reflective metasurface. Section III provides simulation results of the designed dual-channel shared-aperture reflective metasurface and four-channel shared-aperture reflective metasurface. Electric field distributions of the generated vortex beams with single OAM mode and multiple OAM-mode combinations are illustrated, and the corresponding OAM-mode spectra are analyzed. The experimental part is given in Section IV. The dual-channel reflective metasurface are fabricated and measured, and the corresponding vortex-beam electric field distributions and OAM-mode spectra are presented. The measurement results are consistent with the simulations. Moreover, two identical dual-channel reflective metasurfaces are, respectively, applied as the transmitter and receiver for two different OAM-mode vortex-beam multiplexing and demultiplexing transmission experiments, and the transmission coefficients between different OAM-mode combinations are measured.

II. PRINCIPLE AND SIMULATION MODEL

The basic design principle of multichannel shared-aperture reflective metasurface is presented in Fig. 1, which can realize multiple OAM-mode multiplexing and

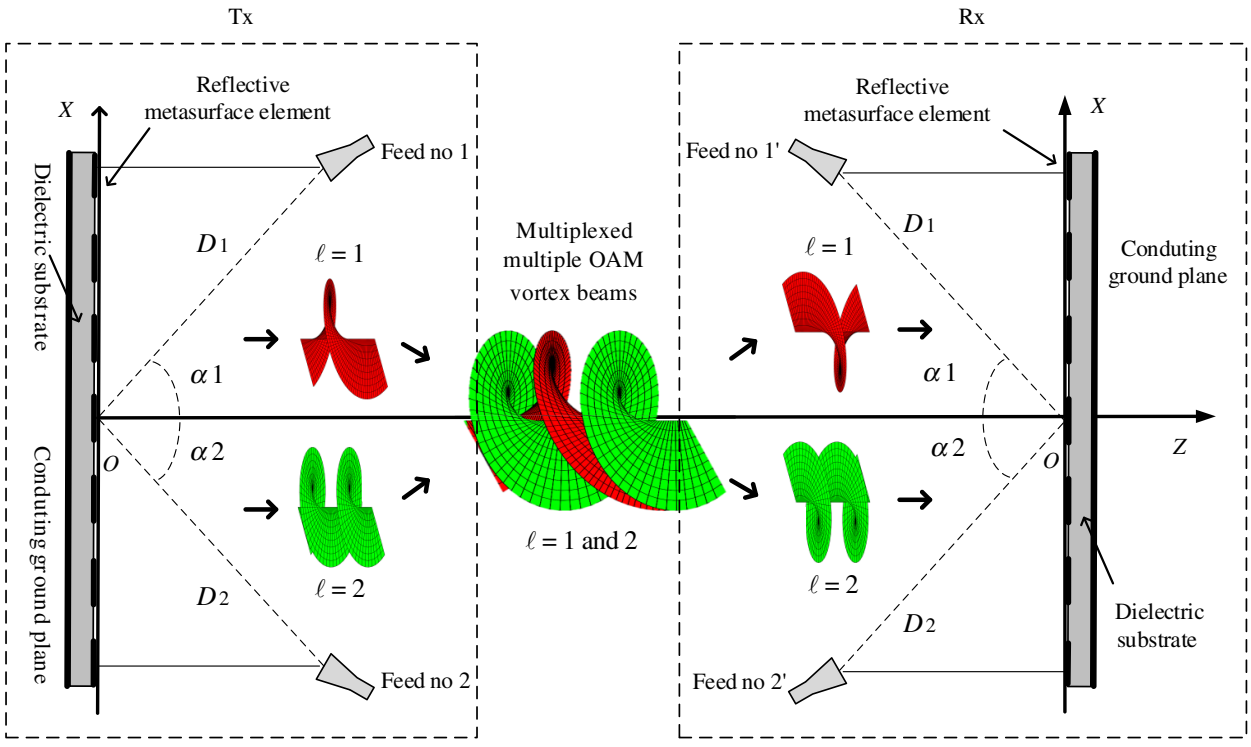

FIG. 1. Schematic diagram of multiple OAM-mode multiplexing and demultiplexing through the multichannel shared-aperture reflective metasurface. A dual-channel model that can multiplex and demultiplex two OAM modes of $\ell = 1$ and 2 is used as an example. Feed horns are used as the data input channels. D_1 and D_2 are distances between the feed horns and the coordinate system's origin. $\alpha 1$ and $\alpha 2$ are angles between the feed horns and z axis.

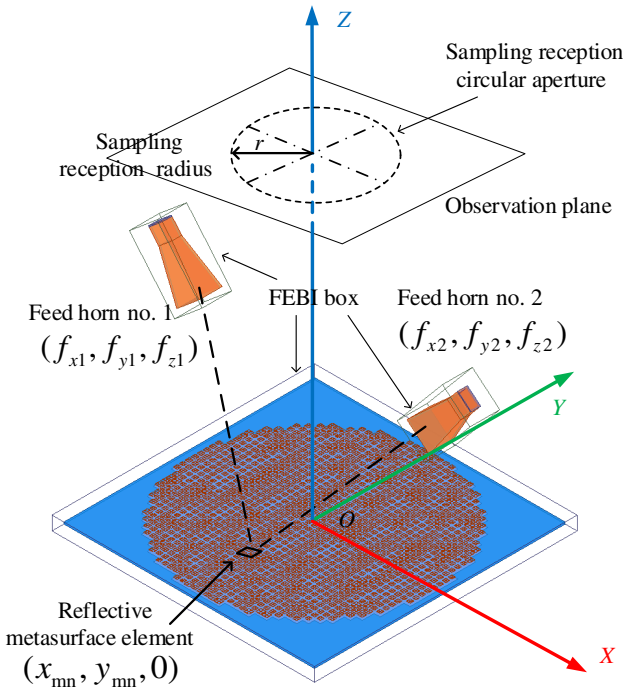

FIG. 2. EM simulation model of the dual-channel shared-aperture reflective metasurface and the corresponding parameter configurations. The generated vortex beam's electric field distributions are obtained in the observation plane perpendicular to z axis, and the geometry center of the observation plane is at z axis. Sampling reception circular aperture located in the observation plane is a circumference with certain radius of r, i.e., sampling reception radius. (f_{x1},f_{y1},f_{z1}) and (f_{x2},f_{y2},f_{z2}) are positions of the feed horns reflectively. The FEBI box is the corresponding EM boundary-condition settings in the EM simulation model.

demultiplexing. The compensation-phase calculation process of the designed metasurface is derived in detail, and a subwavelength unit cell is designed as the metasurface array element. Subsequently, as an example, a dual-channel shared-aperture reflective metasurface is designed to multiplex two different OAM modes of $\ell = 1$ and $\ell = 2$ simultaneously. The corresponding EM simulation model is built by the EM simulation software high-frequency structure simulator (HFSS).

As shown in Fig. 1, the left multichannel shared-aperture metasurface is used as the transmitter for generating the multiplexed multiple OAM-mode vortex beams, and the right metasurface is used as the receiver for separating the different OAM modes. It should be mentioned that the multiplexed and demultiplexed OAM modes $\ell =$ 1 and 2 adopted here are just illustration examples. In fact, this scheme can be extended to more OAM-mode multiplexing and demultiplexing, which means that more channels can be used for more OAM-mode multiplexing and demultiplexing. Considering the reciprocity principle of transmitting and receiving, here we mainly introduce the multiple OAM-mode multiplexing generation method, i.e., transmitting.

In Fig. 2, it is a real dual-channel shared-aperture reflective metasurface EM simulation model. To generate the vortex beam with superposed multiple OAM modes, the tangential electric field on the reflective metasurface can be written as the following simplified form:

$$\begin{aligned} E_R(x_{mn},y_{mn}) &= A_R(x_{mn},y_{mn})e^{j\,\psi_R(x_{mn},y_{mn})} \\ &= \sum_{i=1}^{N} A_i(x_{mn},y_{mn})e^{j\,\psi_i(x_{mn},y_{mn})} \\ &= \sum_{i=1}^{N} A_i(x_{mn},y_{mn})e^{j\,\phi_i(x_{mn},y_{mn})} \times e^{j\,\ell_i\varphi(x_{mn},y_{mn})}, \end{aligned} \tag{1}$$

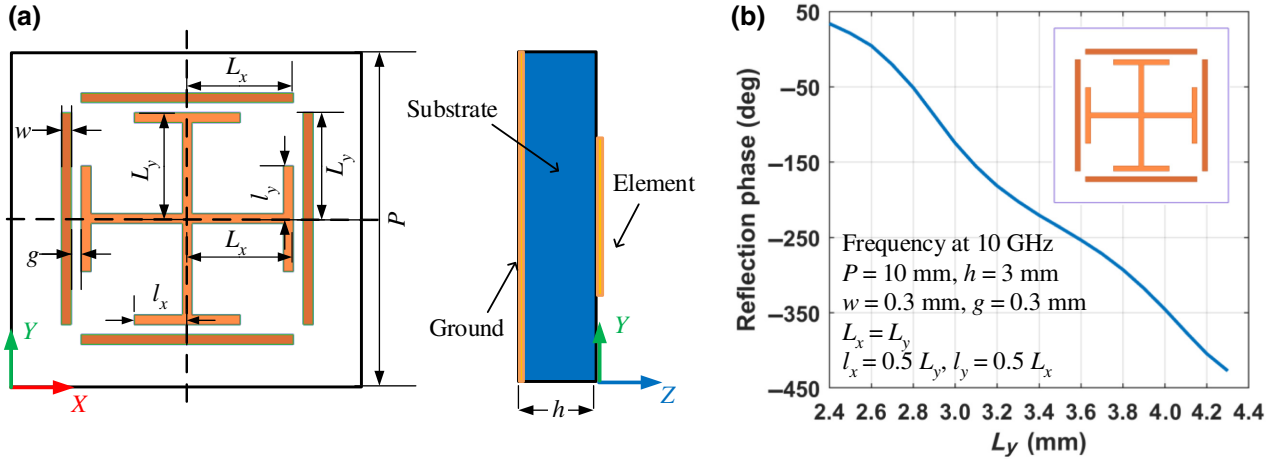

FIG. 3. Unit-cell model of the reflective metasurface array element and its reflection phase response curve. (a) Geometry structure and parameter configurations of the cell. The substrate used here is F4B with $\epsilon_r = 2.65$. (b) Reflection phase response varying with L_y at 10 GHz, and the specific size of the cell.

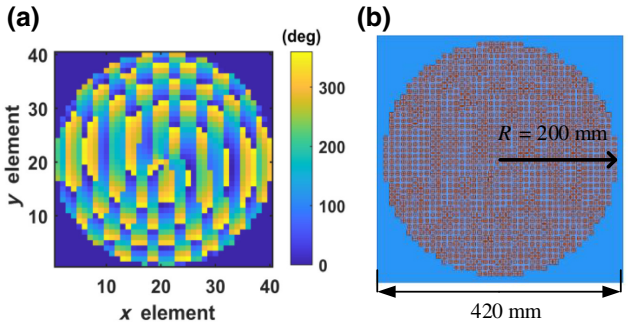

FIG. 4. (a) Calculated compensation phase distribution of the dual-channel reflective metasurface, and (b) the layout model of the designed reflective metasurface based on the calculated compensation phase.

where A_R and ψ_R are the required electric field amplitude and phase distributions of the reflective metasurface array element at the position of $(x_{mn}, y_{mn}, 0)$, and the subscript m and n mean the m_{th} row and the n_{th} column of the reflective metasurface array. A_i and ψ_i are the required electric field amplitude and phase distributions of the reflective metasurface array for generating the vortex beam with OAM mode ℓ_i, and N is the number of the multiplexed OAM modes. $\varphi(x_{mn}, y_{mn})$ is the corresponding azimuthal position of the reflective metasurface array element. Note that the reflective metasurface is placed on the x-o-z plane wherein $z = 0$, and the z-coordinate component is omitted here.

In Eq. (1), $\phi_i(x_{mn}, y_{mn})$ is the compensation phase item for producing a deflected beam in the direction of (θ_b, φ_b), and it can be expressed as [52]

$$\phi_i(x_{mn}, y_{mn}) = kd_i - k\sin\theta_b(x_{mn}\cos\varphi_b + y_{mn}\sin\varphi_b), \tag{2}$$

where k is wave number. d_i is the distance between the feed horn and the reflective metasurface array elements, which can be calculated as follows:

$$d_i = \sqrt{(f_{xi} - x_{mn})^2 + (f_{yi} - y_{mn})^2 + f_{zi}^2}, \tag{3}$$

where (f_{xi}, f_{yi}, f_{zi}) is the position of the i_{th} feed source.

Note that the amplitude distribution $A_i(x_{mn}, y_{mn})$ of the reflective metasurface is generally considered as uniform, and the total compensation phase distribution is obtained as

$$\psi_R(x_{mn}, y_{mn}) = \arg\left\{\sum_{i=1}^{N} A_i(x_{mn}, y_{mn}) e^{j\psi_i(x_{mn}, y_{mn})}\right\}, \tag{4}$$

where the function arg(X) means the argument of a complex number. Meanwhile, the required electric field amplitude distribution of $A_R(x_{mn}, y_{mn})$ in Eq. (1) is also

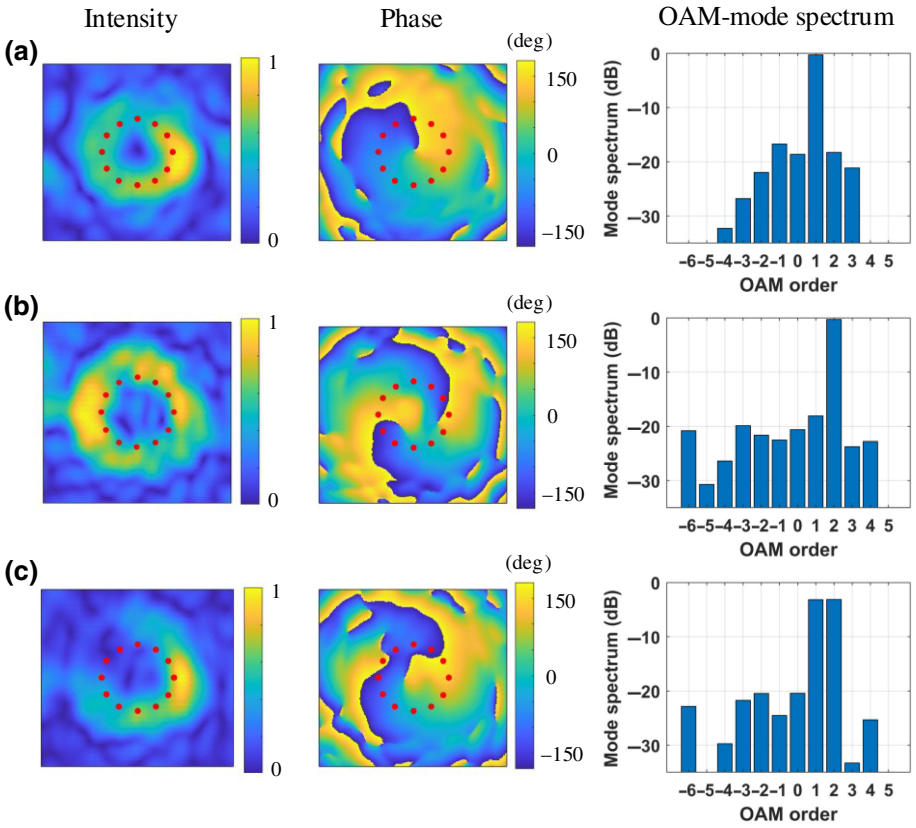

FIG. 5. Simulated vortex electric field intensity distributions and phase distributions in the observation plane, and the calculated OAM-mode spectra under three different cases. The observation plane is set at $z = 700$ mm with a size of 500×500 mm^2. The red circumference is constituted by 12 equally distributed sampling points in sampling reception circular aperture with a reception radius of $r = 95$ mm, which is applied in all these three cases. (a) Case 1, OAM mode $\ell = 1$. (b) Case 2, OAM mode $\ell = 2$. (c) Case 3, two OAM modes of $\ell = 1$ and 2.

considered approximately as uniform, which will cause a high side lobe to some extent, but this can be further optimized through a phase-only synthesis method and other optimization methods [52]. In addition, here we mainly focus on the realization of multiple OAM-mode multiplexing and demultiplexing in the near-field area, and these approximations are acceptable for its design convenience.

The unit-cell model of the designed reflective metasurface array element, which is a Jerusalem form but also a subwavelength element [53], is shown in Fig. 3. The working frequency designed here is 10 GHz corresponding to a working wavelength of $\lambda = 30$ mm, and the polarization of EM wave is linear along the y-axis direction. By varying the length L_y of the unit cell, the corresponding reflective phase response of the array element is realized. Then, according to Eq. (4), the compensation phase of the reflective metasurface is calculated as shown in Fig. 4, in which the final realized layout model of the reflective metasurface is also presented. The size of the reflective metasurface is 420×420 mm^2 while a circular aperture area is applied as the reflective surface. The radius of the circular array is $R = 200$ mm, which corresponds to a 20-array-element arrangement. Finally, the whole EM simulation model is built as shown in Fig. 2. Feed horn no. 1 is used as a data channel for generating vortex beam with OAM mode $\ell = 1$ while feed horn no. 2 is used as another data channel for generating vortex beam with OAM mode $\ell = 2$. The angles between the two feed horns and the z axis are equally set as $\alpha_1 = \alpha_2 = \alpha = 40^\circ$, and the values of D_1 and D_2 are equally 300 mm. Thus, the positions of these two feed horns of (f_{x1}, f_{y1}, f_{z1}) and (f_{x2}, f_{y2}, f_{z2}) are determined.

III. SIMULATION RESULTS AND ANALYSES

In this section, first we simulate the electric field distribution of the dual-channel reflective metasurface in the observation plane. Both the vortex beam's electric intensity distributions and electric field phase distributions are given under different OAM-mode multiplexing combinations. Simultaneously, based on the obtained electric field data, we calculate and analyze their OAM-mode spectra through the whole circular aperture sampling reception method [54]. Then, the other four-channel shared-aperture reflective metasurface that can multiplex four different OAM modes of $\ell = -1, \ell = +1, \ell = -2, \ell = +1$ is also designed. Its EM full-wave simulation model, vortex electric field distributions, and the corresponding OAM-mode spectra are also exhibited, calculated, and analyzed.

We simulate the electric field intensity distributions and phase distributions in the observation plane under three different cases, as shown in Fig. 5. At the same time, their OAM-mode spectra are analyzed, and all these OAM-mode spectra are calculated by normalizing the

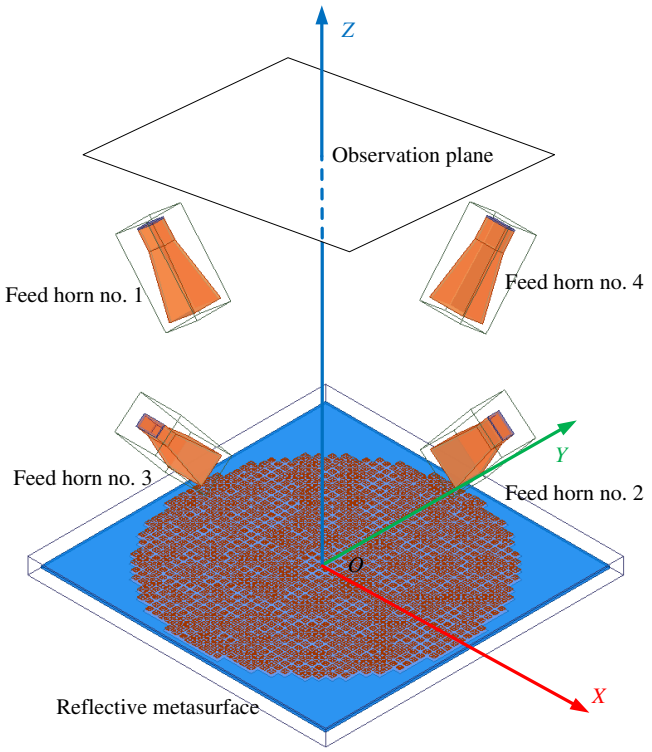

FIG. 6. Full-wave EM simulation model of the four-channel shared-aperture reflective metasurface that realizes four different OAM-mode multiplexing of $\ell = -1, \ell = +1, \ell = -2, \ell = +2$. Feed horn no. 1 channel generates OAM mode $\ell = -1$, feed horn no. 2 channel generates OAM mode $\ell = +1$, feed horn no. 3 channel generates OAM mode $\ell = -2$, and feed horn no. 4 channel generates OAM mode $\ell = +2$.

corresponding OAM-mode spectra's power sum. Note that in Fig. 5 the electric field intensity distributions are all normalized by the maximum value, and the phase distributions all change from -180° to $+180^\circ$. From the simulation results in Fig. 5, we can see that although the simulated vortex electric field distributions undergo some distortions, through calculating the OAM-mode spectrum

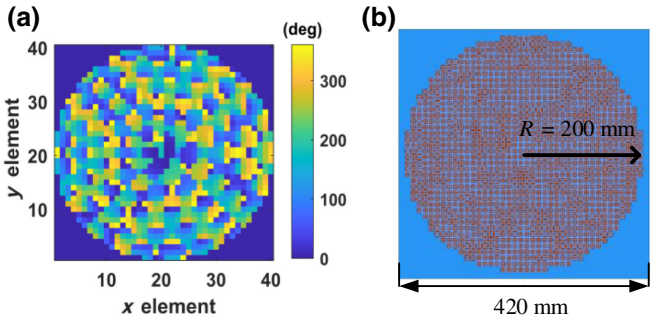

FIG. 7. (a) Calculated compensation phase distributions of the four-channel reflective metasurface, and (b) the simulation model's layout of the four-channel reflective metasurface.

distributions, the corresponding OAM modes can still be distinguished clearly, and the mode purities of different OAM modes keep well. The multiplexed OAM modes hold at least 15 dB higher than the other crosstalk modes. Hence it proves the feasibility of our proposed multiple OAM-mode multiplexing scheme.

To further verify the effectiveness of our method, we design another four-channel reflective metasurface that can multiplex four different OAM modes, as shown in Fig. 6. The positions of feed horns no. 1 and no. 2 are the same as the previous dual-channel reflective metasurface model shown in Fig. 2; while feed horns no. 3 and no. 4 are located in the y-o-z plane, and their positions are obtained by rotating the feed horns no. 1 and no. 2 around the z axis with 90° clockwise. The size and other related parameters and configurations of the four-channel reflective surface are the same as those of the previous dual-channel reflective metasurface model.

Similarly, according to Eq. (4) the calculated compensation phase distributions and the reflective metasurface's layout of the four-channel reflective metasurface are shown in Fig. 7. When the corresponding feed-horn channel is excited, the corresponding OAM mode is multiplexed. Four feed-horn-channel excitations lead to four OAM modes multiplexing. We simulate the corresponding electric field distributions of the four-channel reflective metasurface as shown in Fig. 8, in which these four different multiplexing cases are analyzed. From the simulated electric field distributions and the corresponding OAM-mode spectrum analyses, clearly, the four OAM-mode

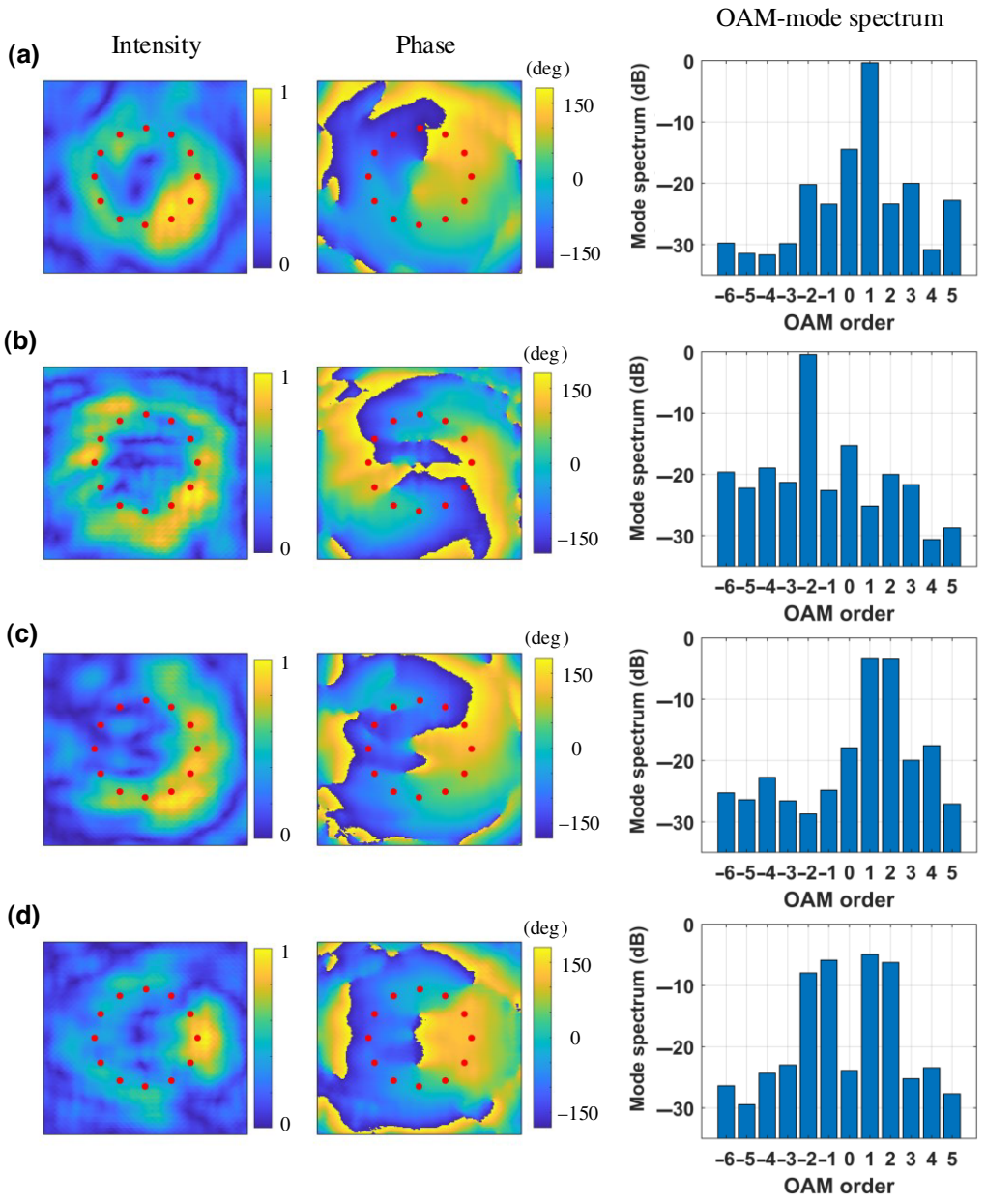

FIG. 8. Simulated vortex electric field intensity distributions and phase distributions, and the calculated OAM-mode spectra under four different cases. The observation plane is set at $z = 600$ mm with the size of 400×400 mm^2. The red circumference is constituted by 12 equally distributed sampling points in sampling reception circular aperture with a reception radius of $r = 104$ mm, which is applied in all four cases. (a) Case 1, OAM mode $\ell = 1$. (b) Case 2, OAM mode $\ell = -2$. (c) Case 3, two OAM modes of $\ell = 1$ and 2. (d) Case 4, four OAM modes of $\ell = \pm 1$ and $\ell = \pm 2$.

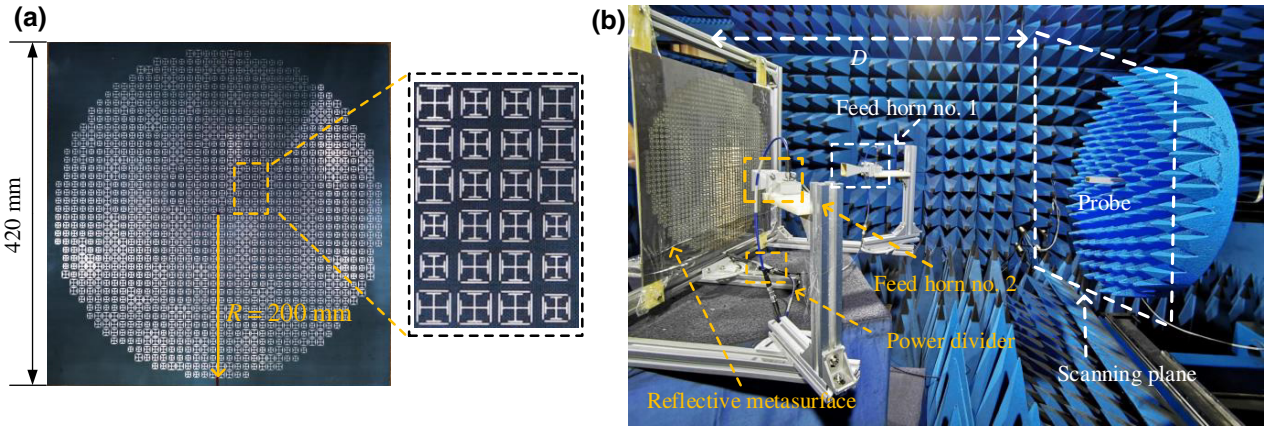

FIG. 9. (a) Fabricated prototype of the dual-channel shared-aperture reflective metasurface. (b) Measurement environment in a microwave chamber under near-field scanning. Two feed horns are connected by a two-way power divider module through radio-frequency cables to realize simultaneous excitation. The distance between the reflective metasurface and the measurement scanning plane is $D = 700$ mm, and the size of the scanning plane is 500×500 mm^2.

multiplexing scheme is also feasible, and the multiplexed OAM modes can still hold at nearly 15 dB higher than other crosstalk modes.

IV. MEASUREMENT RESULTS AND ANALYSIS

In this section, the dual-channel reflective metasurface is fabricated and measured. Subsequently, two identical dual-channel reflective metasurfaces are applied for multiple OAM mode vortex-beam multiplexing and demultiplexing wireless-transceiver experiments. Note that here we mainly measure the transmission coefficients of the demultiplexed radio-frequency carrier wave between the different feed-horn ports, and do not consider the baseband signal modulation.

In Fig. 9(a) it is the fabricated prototype, and in Fig. 9(b) it is the corresponding measurement environment. Similar to the simulation situation, we measure the vortex electric

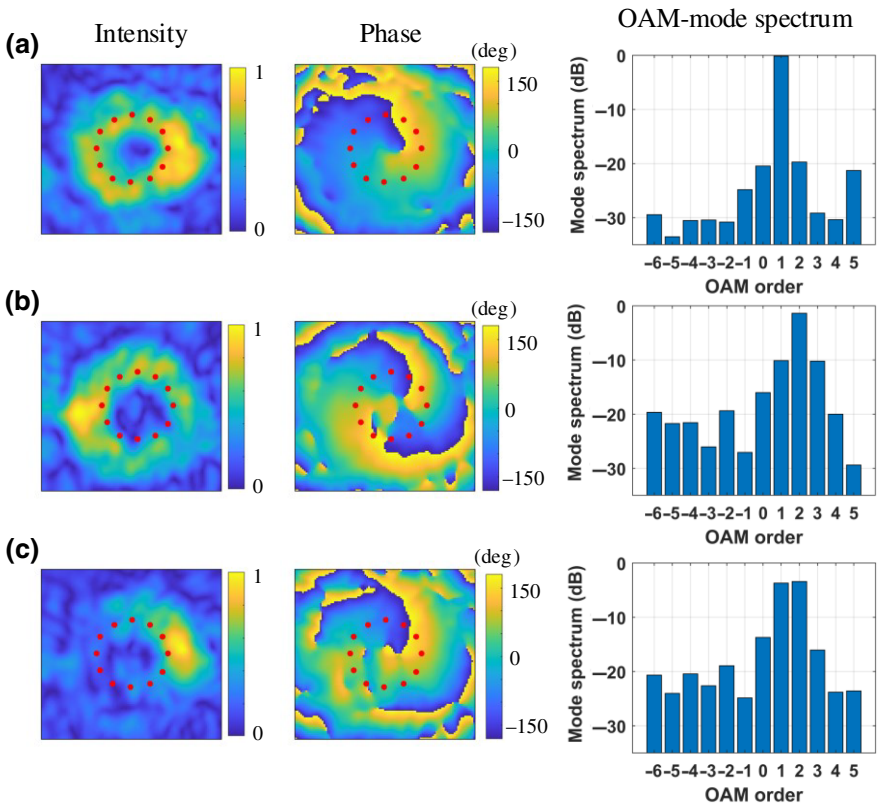

FIG. 10. Measured vortex electric field intensity distributions and electric field phase distributions, and the calculated OAM-mode spectra under three different cases. The red circumference is constituted by 12 equally distributed sampling points in the sampling reception circular aperture with a reception radius of $r = 50$ mm, which is applied in all these three cases. (a) Case 1, OAM mode $\ell = 1$. (b) Case 2, OAM mode $\ell = 2$. (c) Case 3, multiplexed multiple OAM modes $\ell = 1$ and 2.

field intensity distributions and the vortex electric field phase distributions in the scanning plane under a testing frequency of 10 GHz, corresponding to the wavelength of $\lambda = 30$ mm. Three different cases are measured, i.e., single OAM mode $\ell = 1$, $\ell = 2$, and multiplexed OAM modes of $\ell = 1$ and 2, respectively. The measured vortex electric field distributions are shown in Fig. 10, and the corresponding OAM-mode spectra are calculated and analyzed.

The measured vortex electric field distributions in Fig. 10 and the simulated electric field distributions in Fig. 5 hold basically consistent. As shown in Fig. 10, the measured multiplexed OAM modes realize at least 8.5 dB higher than other crosstalk OAM modes in all these three cases discussed above. The prototype's manufacture errors constitute part of the measurement errors, and antenna alignment is another factor that impacts on the vortex-beam measurement qualities. Although the measured vortex electric field distributions and the corresponding OAM-mode spectra are not as well as the simulated results, the majority of multiplexed OAM modes can be successfully distinguished.

Subsequently, based on the fabricated prototype of the dual-channel shared-aperture reflective metasurface as shown in Fig. 9, two identical prototypes are used as the transmitter and receiver, respectively, for multiple OAM mode vortex-beam multiplexing and demultiplexing wireless-transceiver experiments. Fig. 11 shows the corresponding measurement environment. By measuring the transmission coefficients between the different feed-horn port channels, the corresponding multiplexed and demultiplexed OAM modes are measured.

Four different groups of measurement data are obtained under four different transmission distances, and the corresponding measurement results are presented in Fig. 12. Note that because of the reciprocity principle property, the measurement curves of $S(1,2)$ and $S(2,1)$ are nearly overlapped. From the measurement results in Fig. 12, it is obvious that in the working frequency band around 10 GHz, the matched OAM-mode transmission level, i.e., $S(1,1)$ and $S(2,2)$, can keep at least 10 dB higher than the mismatched OAM-mode transmission level, i.e., $S(2,1)$ and $S(1,2)$. The orthogonalities between different OAM modes are maintained well to a certain extent. This transceiver experiment also further verifies the feasibilities of the shared-aperture reflective-metasurface-based OAM-mode multiplexing and demultiplexing scheme of vortex beam. Moreover, in practical applications, the operating bandwidth of this multiple OAM-mode transceiver system is related to the operating bandwidth of the designed metasurface to a certain extent [55].

In this paper, the simulation and experimental demonstrations are finished under a short transmission distance, which is because of the inherent beam-divergence characteristics of OAM vortex beams. When the transmission distance becomes longer, the transmission quality of OAM vortex wave multiplexing will be affected, and its transmission power level will become lower. As shown in Fig. 12, as the transmission distance increases, the transmission coefficient between the transmitter and the receiver shows a decreasing trend. Furthermore, we hold the view that at the current research stage in this field, OAM vortex waves are more suitable for near-field related application scenarios. Additionally, in practical applications, the environmental turbulence will also affect OAM multiplexing transmission, and especially high-order OAM modes are more sensitive to environmental turbulence [56]. There have been many related research works about this issue [57–59], which are also useful and meaningful to the practical applications of OAM vortex waves.

Furthermore, as mentioned at the beginning of the paper, our proposed multi-OAM-mode multiplexing and demultiplexing scheme can be extended to more OAM-mode applications. However, in practical implementations, larger metasurface structure is necessary if more OAM modes are multiplexed and demultiplexed. A finite metasurface structure will limit and affect more OAM modes

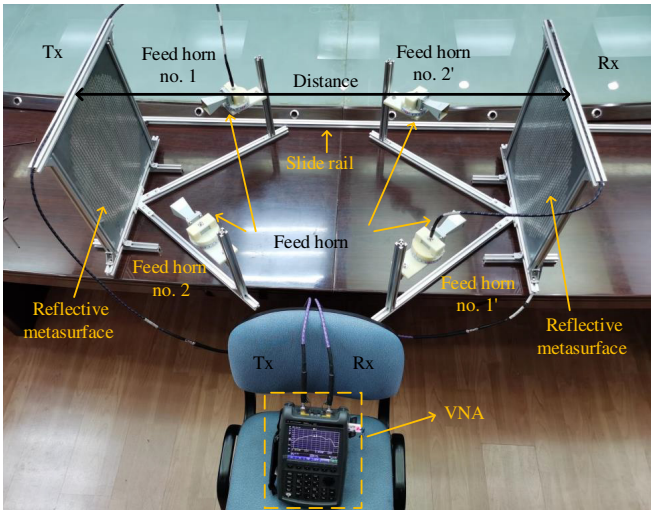

FIG. 11. Measurement environment for multiple OAM-mode vortex-beam multiplexing and demultiplexing wireless-transceiver experiments. The left dual-channel shared-aperture reflective metasurface is used as the transmitter, which multiplexes the OAM modes of $\ell = 1$ and $\ell = 2$. The feed horn no. 1 channel corresponds to the OAM mode $\ell = 1$ while the feed horn no. 2 channel corresponds to the OAM mode $\ell = 2$. The right dual-channel shared-aperture reflective metasurface is used as the receiver, which demultiplexes the OAM modes of $\ell = 1$ and $\ell = 2$. The feed horn no. 1' channel corresponds to the OAM mode $\ell = 1$ while the feed horn no. 2' channel corresponds to the OAM mode $\ell = 2$. The vector network analyzer (VNA) is used for measuring the transmission coefficients between the different feed-horn ports. The side rail is used for adjusting the distance between the transmitter and receiver.

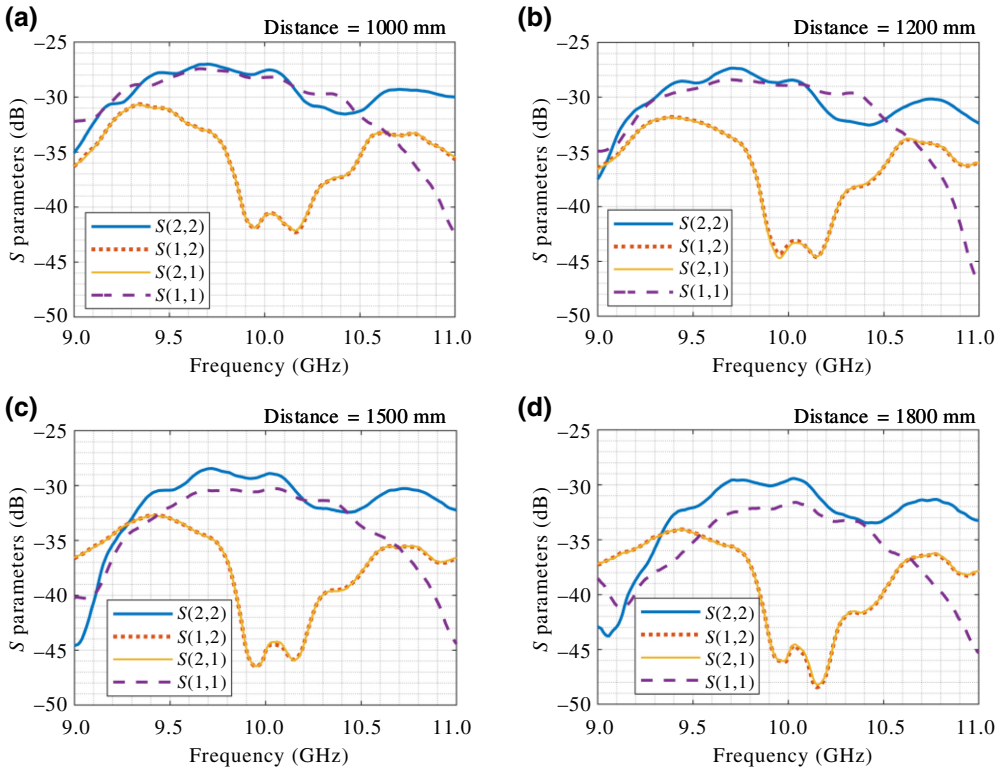

FIG. 12. Measurement results of the transmission coefficients between different feed-horn port channels under different distances. Parameters $S(2,2)$ and $S(1,1)$ mean the transmission coefficients between the same OAM modes of $\ell = 1$ or $\ell = 2$, while parameters $S(2,1)$ and $S(1,2)$ mean the transmission coefficients between different OAM modes of $\ell = 1$ and $\ell = 2$, respectively. Four different distances between Tx and Rx are measured, i.e., 1000 mm (approximately 33.3λ), 1200 mm (40λ), 1500 mm (50λ), and 1800 mm (60λ).

multiplexing. The differences between the realistic metasurface model and the ideal metasurface model should be considered. When more OAM modes are multiplexed, the impact of the approximate design errors introduced by the realistic metasurface model turns to be more evident, and it will make the crosstalks between different OAM modes more serious.

V. CONCLUSIONS

We propose a multiple OAM-mode vortex-beam multiplexing and demultiplexing scheme based on the shared-aperture reflective metasurface. The dual-channel reflective metasurface for two OAM-mode multiplexing and four-channel reflective metasurface for four OAM-mode multiplexing are investigated, respectively, as two examples. The corresponding vortex electric field distributions and OAM-mode spectra are analyzed. The dual-channel reflective metasurface is fabricated and measured, which further proves the effectiveness of our multiplexing method. Moreover, on the basis of the designed dual-channel shared-aperture reflective metasurface, the corresponding transceiver experiments for the multiple OAM-mode vortex-beam multiplexing and demultiplexing tests are carried out. This shared-aperture reflective-metasurface-based multiple OAM-mode multiplexing and demultiplexing scheme can further promote the development of the OAM multiplexing and demultiplexing technology, and its applications in the wireless communications. In the future, this OAM multiplexing and demultiplexing scheme can also be extended to IRS and information metamaterial systems.

ACKNOWLEDGMENTS

This work is supported by National Key R&D Program of China, and by Innovation Capability Support Program of Shaanxi (Program No. 2021TD-07). T.J.C. acknowledges the supports from the National Key Research and Development Program of China under Grants No. 2021YFA1401001, No. 2017YFA0700201, No. 2017YFA0700202, and No. 2017YFA0700203, and the 111 Project under Grant No. 111-2-05.

[1] L. Allen, M. W. Beijersbergen, R. J. C. Spreeuw, and J. P. Woerdman, Orbital angular momentum of light and the transformation of Laguerre-Gaussian laser modes, Phys. Rev. A **45**, 8185 (1992).

[2] B. Thidé, H. Then, J. Sjöholm, K. Palmer, J. Bergman, T. D. Carozzi, Y. N. Istomin, N. H. Ibragimov, and R. Khamitova, Utilization of Photon Orbital Angular Momentum in the Low-Frequency Radio Domain, Phys. Rev. Lett. **99** 087701 (2007).

[3] D. LEE, H. SASAKI, H. FUKUMOTO, K. HIRAGA, and T. NAKAGAWA, Orbital angular momentum (OAM) multiplexing: An enabler of a new era of wireless communications, IEICE Trans. Commun. **E100.B**, 1044 (2017).

[4] A. E. Willner, Y. Ren, G. Xie, Y. Yan, L. Li, Z. Zhao, J. Wang, M. Tur, A. F. Molisch, and S. Ashrafi, Recent

advances in high-capacity free-space optical and radio-frequency communications using orbital angular momentum multiplexing, Philos. Trans. R. Soc. A: Math. Phys. Eng. Sci. **375**, 20150439 (2017).

[5] R. Chen, H. Zhou, M. Moretti, X. Wang, and J. Li, Orbital angular momentum waves: Generation, detection, and emerging applications, IEEE Commun. Surveys Tutorials **22**, 840 (2020).

[6] A. E. Willner and C. Liu, Perspective on using multiple orbital-angular-momentum beams for enhanced capacity in free-space optical communication links, Nanophotonics **10**, 225 (2020).

[7] F. Tamburini, E. Mari, A. Sponselli, B. Thidé, A. Bianchini, and F. Romanato, Encoding many channels on the same frequency through radio vorticity: First experimental test, New J. Phys. **14**, 033001 (2012).

[8] W. Zhang, S. Zheng, X. Hui, R. Dong, X. Jin, H. Chi, and X. Zhang, Mode division multiplexing communication using microwave orbital angular momentum: An experimental study, IEEE Trans. Wirel. Commun. **16**, 1308 (2017).

[9] J. Wang, J.-Y. Yang, I. M. Fazal, N. Ahmed, Y. Yan, H. Huang, Y. Ren, Y. Yue, S. Dolinar, M. Tur, and A. E. Willner, Terabit free-space data transmission employing orbital angular momentum multiplexing, Nat. Photonics **6**, 488 (2012).

[10] Y. Yagi, H. Sasaki, T. Semoto, T. Kageyama, T. Yamada, J. Mashino, and D. Lee, in *2021 IEEE International Conference on Communications Workshops (ICC Workshops)* (2021), p. 1.

[11] Y. Ren, L. Li, G. Xie, Y. Yan, Y. Cao, H. Huang, N. Ahmed, Z. Zhao, P. Liao, C. Zhang, G. Caire, A. F. Molisch, M. Tur, and A. E. Willner, Line-of-sight millimeter-wave communications using orbital angular momentum multiplexing combined with conventional spatial multiplexing, IEEE Trans. Wirel. Commun. **16**, 3151 (2017).

[12] A. Trichili, K.-H. Park, M. Zghal, B. S. Ooi, and M.-S. Alouini, Communicating using spatial mode multiplexing: Potentials, challenges, and perspectives, IEEE Commun. Surveys Tutorials **21**, 3175 (2019).

[13] O. Edfors and A. J. Johansson, Is orbital angular momentum (OAM) based radio communication an unexploited area?, IEEE Trans. Antennas Propag. **60**, 1126 (2012).

[14] M. Oldoni, F. Spinello, E. Mari, G. Parisi, C. G. Someda, F. Tamburini, F. Romanato, R. A. Ravanelli, P. Coassini, and B. Thide, Space-division demultiplexing in orbital-angular-momentum-based MIMO radio systems, IEEE Trans. Antennas Propag. **63**, 4582 (2015).

[15] C. Zhang, J. Jiang, Y. Zhao, and X. Jiang, in *2019 IEEE Globecom Workshops (GC Wkshps)* (IEEE, 2019).

[16] G. Gibson, J. Courtial, M. J. Padgett, M. Vasnetsov, V. Pas'ko, S. M. Barnett, and S. Franke-Arnold, Free-space information transfer using light beams carrying orbital angular momentum, Opt. Express **12**, 5448 (2004).

[17] B. Allen, A. Tennant, Q. Bai, and E. Chatziantoniou, Wireless data encoding and decoding using OAM modes, Electron. Lett. **50**, 232 (2014).

[18] D. Cozzolino, B. D. Lio, D. Bacco, and L. K. Oxenløwe, High-dimensional quantum communication: Benefits, progress, and future challenges, Adv. Quantum Technol. **2**, 1900038 (2019).

[19] K. Liu, Y. Cheng, X. Li, and Y. Jiang, Passive oam-based radar imaging with single-in-multiple-out mode, IEEE Microw. Wirel. Compon. Lett. **28**, 840 (2018).

[20] K. Liu, Y. Cheng, X. Li, and Y. Gao, Microwave-sensing technology using orbital angular momentum: Overview of its advantages, IEEE Veh. Technol. Mag. **14**, 112 (2019).

[21] K. Liu, Y. Cheng, H. Liu, and H. Wang, Computational imaging with low-order oam beams at microwave frequencies, Sci. Rep. **10**, 11641 (2020).

[22] M. Barbuto, A. Bassotti, A. Alù, F. Bilotti, and A. Toscano, in *2021 Fifteenth International Congress on Artificial Materials for Novel Wave Phenomena (Metamaterials)* (2021), p. 035.

[23] M. Barbuto, A. Alù, F. Bilotti, and A. Toscano, Dual-circularly polarized topological patch antenna with pattern diversity, IEEE Access **9**, 48769 (2021).

[24] M. Tamagnone, C. Craeye, and J. Perruisseau-Carrier, Comment on 'encoding many channels on the same frequency through radio vorticity: First experimental test', New J. Phys. **14**, 118001 (2012).

[25] F. Tamburini, B. Thidé, E. Mari, A. Sponselli, A. Bianchini, and F. Romanato, Reply to comment on 'encoding many channels on the same frequency through radio vorticity: First experimental test', New J. Phys. **14**, 118002 (2012).

[26] M. Tamagnone, C. Craeye, and J. Perruisseau-Carrier, Comment on 'reply to comment on "encoding many channels on the same frequency through radio vorticity: First experimental test', New J. Phys. **15**, 078001 (2013).

[27] S. Chen, Y.-C. Liang, S. Sun, S. Kang, W. Cheng, and M. Peng, Vision, requirements, and technology trend of 6g: How to tackle the challenges of system coverage, capacity, user data-rate and movement speed, IEEE Wirel. Commun. **27**, 218 (2020).

[28] A. Papathanasopoulos and Y. Rahmat-Samii, in *Electromagnetic Vortices* (John Wiley & Sons, Ltd, 2021), Chap. 1, p. 1.

[29] B. Thidé and F. Tamburini, in *Electromagnetic Vortices* (John Wiley & Sons, Ltd, 2021), Chap. 2, p. 33.

[30] A. M. Yao and M. J. Padgett, Orbital angular momentum: Origins, behavior and applications, Adv. Opt. Photonics **3**, 161 (2011).

[31] M. J. Padgett, Orbital angular momentum 25 years on [invited], Opt. Express **25**, 11265 (2017).

[32] M. Veysi, C. Guclu, F. Capolino, and Y. Rahmat-Samii, Revisiting orbital angular momentum beams: Fundamentals, reflectarray generation, and novel antenna applications, IEEE Antennas Propag. Mag. **60**, 68 (2018).

[33] H. Sasaki, Y. Yagi, T. Yamada, and D. Lee, in *2019 IEEE Globecom Workshops (GC Wkshps)* (IEEE, 2019).

[34] C.-X. Wang, J. Huang, H. Wang, X. Gao, X. You, and Y. Hao, 6g wireless channel measurements and models: Trends and challenges, IEEE Veh. Technol. Mag. **15**, 22 (2020).

[35] J. Xu, Y. Guo, P. Yang, R. Zhang, X. Zhai, S. Huang, and K. Bi, Recent progress on RF orbital angular momentum antennas, J. Electromagn. Waves Appl. **34**, 275 (2020).
[36] N. Yu, P. Genevet, M. A. Kats, F. Aieta, J.-P. Tetienne, F. Capasso, and Z. Gaburro, Light propagation with phase discontinuities: Generalized laws of reflection and refraction, Science **334**, 333 (2011).
[37] F. Aieta, P. Genevet, N. Yu, M. A. Kats, Z. Gaburro, and F. Capasso, Out-of-plane reflection and refraction of light by anisotropic optical antenna metasurfaces with phase discontinuities, Nano Lett. **12**, 1702 (2012).
[38] T. J. Cui, Microwave metamaterials, Natl. Sci. Rev. **5**, 134 (2017).
[39] S. Yu, L. Li, G. Shi, C. Zhu, X. Zhou, and Y. Shi, Design, fabrication, and measurement of reflective metasurface for orbital angular momentum vortex wave in radio frequency domain, Appl. Phys. Lett. **108**, 121903 (2016).
[40] S. Yu, L. Li, G. Shi, C. Zhu, and Y. Shi, Generating multiple orbital angular momentum vortex beams using a metasurface in radio frequency domain, Appl. Phys. Lett. **108**, 241901 (2016).
[41] S. Yu, L. Li, and N. Kou, Generation, reception and separation of mixed-state orbital angular momentum vortex beams using metasurfaces, Opt. Mater. Express **7**, 3312 (2017).
[42] M. Chen, L. Jiang, and W. Sha, Orbital angular momentum generation and detection by geometric-phase based metasurfaces, Appl. Sci. **8**, 362 (2018).
[43] J. Han, L. Li, H. Yi, and Y. Shi, 1-bit digital orbital angular momentum vortex beam generator based on a coding reflective metasurface, Opt. Mater. Express **8**, 3470 (2018).
[44] J. Han, L. Li, H. Yi, and W. Xue, Versatile orbital angular momentum vortex beam generator based on reconfigurable reflective metasurface, Jpn. J. Appl. Phys. **57**, 120303 (2018).
[45] Y. Shuang, H. Zhao, W. Ji, T. J. Cui, and L. Li, Programmable high-order OAM-carrying beams for direct-modulation wireless communications, IEEE J. Emerg. Sel. Top. Circuits Syst. **10**, 29 (2020).
[46] L.-J. Yang, S. Sun, and W. E. I. Sha, Manipulation of orbital angular momentum spectrum using shape-tailored metasurfaces, Adv. Opt. Mater. **9**, 2001711 (2020).
[47] L. Guan, Z. He, D. Ding, Y. Yu, W. Zhang, and R. Chen, Polarization-controlled shared-aperture metasurface for generating a vortex beam with different modes, IEEE Trans. Antennas Propag. **66**, 7455 (2018).
[48] Y. Li, A. Li, and T. jun Cui, Four-channel orbital angular momentum beam multiplexer designed with low-profile metasurfaces, J. Phys. D: Appl. Phys. **52**, 025108 (2018).
[49] G.-B. Wu, K. F. Chan, K. M. Shum, and C. H. Chan, Millimeter-wave holographic flat lens antenna for orbital angular momentum multiplexing, IEEE Trans. Antennas Propag. **69**, 4289 (2021).
[50] T. J. Cui, L. Li, S. Liu, Q. Ma, L. Zhang, X. Wan, W. X. Jiang, and Q. Cheng, Information metamaterial systems, iScience **23**, 101403 (2020).
[51] S. Gong, X. Lu, D. T. Hoang, D. Niyato, L. Shu, D. I. Kim, and Y.-C. Liang, Toward smart wireless communications via intelligent reflecting surfaces: A contemporary survey, IEEE Commun. Surveys Tutorials **22**, 2283 (2020).
[52] J. Huang, *Reflectarray Antenna* (John Wiley & Sons, Hoboken, New Jersey, 2007).
[53] G.-B. Wu, S.-W. Qu, S. Yang, and C. H. Chan, Broadband, single-layer dual circularly polarized reflectarrays with linearly polarized feed, IEEE Trans. Antennas Propag. **64**, 4235 (2016).
[54] Q. Feng, J. Liang, and L. Li, Variable scale aperture sampling reception method for multiple orbital angular momentum modes vortex wave, IEEE Access **7**, 158847 (2019).
[55] L.-J. Yang, S. Sun, and W. E. I. Sha, Ultrawideband reflection-type metasurface for generating integer and fractional orbital angular momentum, IEEE Trans. Antennas Propag. **68**, 2166 (2020).
[56] X. Yan, P.-F. Zhang, C.-Y. Fan, and J.-H. Zhang, Effect of atmospheric turbulence on orbital angular momentum entangled state, Commun. Theor. Phys. **74**, 025102 (2022).
[57] Y. Ren, G. Xie, H. Huang, C. Bao, Y. Yan, N. Ahmed, M. P. J. Lavery, B. I. Erkmen, S. Dolinar, M. Tur, M. A. Neifeld, M. J. Padgett, R. W. Boyd, J. H. Shapiro, and A. E. Willner, Adaptive optics compensation of multiple orbital angular momentum beams propagating through emulated atmospheric turbulence, Opt. Lett. **39**, 2845 (2014).
[58] Y. Zhang, P. Wang, L. Guo, W. Wang, and H. Tian, Performance analysis of an oam multiplexing-based MIMO FSO system over atmospheric turbulence using space-time coding with channel estimation, Opt. Express **25**, 19995 (2017).
[59] R. Zhang, H. Song, Z. Zhao, H. Song, J. Du, C. Liu, K. Pang, L. Li, H. Zhou, A. N. Willner, A. Almaiman, Y. Zhou, R. W. Boyd, B. Lynn, R. Bock, M. Tur, and A. E. Willner, Simultaneous turbulence mitigation and channel demultiplexing for two 100–gbit/s orbital-angular-momentum multiplexed beams by adaptive wavefront shaping and diffusing, Opt. Lett. **45**, 702 (2020).